45th AIAA Aerospace Sciences Meeting and Exhibit
8 - 11 January 2007, Reno, Nevada

AIAA-2007-0722
45th AIAA Aerospace Science Meeting and Exhibit, Jan. 8-11, Reno, Nevada

Numerical and modeling issues in LES of compressible turbulence on unstructured grids

Noma Park* and Krishnan Mahesh†
University of Minnesota, Minneapolis, MN, 55455, USA

This paper discusses numerical and modeling issues that arise in cell-centered finite-volume methods (FVM) for large eddy simulation (LES) of compressible flows on unstructured grids. These are: accuracy and stability of flux interpolation scheme, shock capturing strategy, and subgrid-scale (SGS) modeling. To enhance the accuracy of flux reconstruction, a new scheme with added first derivative term from each cell center is proposed, and tested for various benchmark problems. It is shown that stability as well as accuracy is determined by the formulation of gradient at cell center. As a shock-capturing method, a characteristic based filter is formulated for cell-centered FVM on unstructured grids. The filter is combined with a sensor based on the local divergence and vorticity. Also, a one-equation subgrid model based on the subgrid kinetic energy transport equation for compressible flows is proposed.

I. Introduction

Upwind schemes and centered difference with artificial dissipation have been popular discretization methods for the Reynolds-Averaged Navier-Stokes (RANS) simulation of compressible flows. However, there is evidence that such schemes might be undesirable for large eddy simulation (LES) due to excessive numerical dissipation.[1–3] Furthermore, in order to handle complex geometries, unstructured grids are preferred. Non-dissipative finite volume schemes on unstructured grids introduce some nontrivial numerical and modeling issues. The present paper considers (i) the accuracy and stability of the base scheme, (ii) shock-capturing scheme and (iii) the SGS model.

The accuracy of the scheme is determined by the flux reconstruction at cell faces. In collocated FVM, simple symmetric average is preferred due to its good quadratic conservation property.[4,5] However, this symmetric average is only first-order accurate, and this degradation of accuracy becomes a serious problem for highly skewed unstructured grids. However, the increase of formal accuracy in the context of unstructured FVM is not straightforward. Also, the introduction of high order interpolation can cause numerical instability.

An external shock-capturing mechanism should be provided for non-dissipative FVM. Possible candidates are Jameson type artificial dissipation,[6] characteristic filtering[7] and combination with upwind scheme such as ENO.[8,9] The key issue is to concentrate numerical dissipation in the vicinity of the flow discontinuity and minimize unnecessary dissipation. Especially, it is important for shock capturing schemes to discriminate between the shock wave and under-resolved turbulence. Even advanced upwind schemes such as WENO do not meet this requirement,[3] and can even laminarize flow when applied to fully developed channel flow.

Finally, we consider issues regarding LES on unstructured grids. The first problem one encounters is that the shape of filter associated with grid is unknown. This fact makes it difficult to compare DNS data with computed LES solution since the exact LES solution is undefined. Another problem arises in the implementation of the dynamic Smagorinsky model (DSM),[10] which is one of the most popular subgrid scale (SGS) models. DSM requires test filtering and averaging over homogeneous, if any, direction(s). However, it is difficult to derive the desired test filter since it is hard to derive the transfer function in the spectral

*Postdoctoral research associate, Aerospace Engineering & Mechanics
†Associate Professor, Aerospace Engineering & Mechanics, AIAA member

space. Also, in incompressible flows, the subgrid kinetic energy is absorbed in the pressure. However, for compressible flows, the subgrid kinetic energy requires explicit modeling.

The objective of the present paper is to propose a numerical method and SGS model which consider the above numerical issues. The paper is organized as follows. In Sec. II, governing equations, finite volume formulation and time integration schemes are summarized. Sec. III deals with numerical issues related with convective and viscous flux reconstruction. The implementation of shock capturing scheme and its performance is evaluated in Sec. IV. Issues regarding SGS model implementation and computational results are presented in Sec. V. The paper is summarized in Sec. VI.

II. Governing equation and finite volume formulation

The governing equations are the spatially filtered continuity, momentum, and total energy conservation equations:

$$\begin{aligned}
\frac{\partial \overline{\rho}}{\partial t} &= -\frac{\partial}{\partial x_k}\left(\overline{\rho u_k}\right), \\
\frac{\partial \overline{\rho}\widetilde{u}_i}{\partial t} &= -\frac{\partial}{\partial x_k}\left(\overline{\rho}\widetilde{u}_i\widetilde{u}_k + \overline{p}\delta_{ik} - \widetilde{\sigma}_{ik} + \tau_{ik}\right), \\
\frac{\partial \overline{E}_T}{\partial t} &= -\frac{\partial}{\partial x_k}\left\{\left(\overline{E}_T + \overline{p}\right)\widetilde{u}_k - \widetilde{\sigma}_{ik}\widetilde{u}_i - \overline{Q}_k + q_k\right\},
\end{aligned} \tag{1}$$

where ρ, u_i, p and E_T are density, velocity, pressure and total energy, respectively. The viscous stress $\widetilde{\sigma_{ij}}$ and heat flux $\overline{Q}_i$ are given by

$$\widetilde{\sigma_{ij}} = \frac{\mu}{Re}\left(\frac{\partial \widetilde{u}_i}{\partial x_j} + \frac{\partial \widetilde{u}_j}{\partial x_i} - \frac{2}{3}\frac{\partial \widetilde{u_k}}{\partial x_k}\delta_{ij}\right), \tag{2}$$

$$\overline{Q}_i = \frac{\mu}{(\gamma-1)M_\infty^2 RePr}\frac{\partial \overline{T}}{\partial x_i} \tag{3}$$

after standard non-dimensionalization, where Re, M_∞ and Pr denote the Reynolds, Mach and Prandtl numbers. For all problems considered in this paper, $\mu = (T/T_{ref})^{0.7}$ and $Pr = 0.72$. Here

$$\overline{\phi}(\mathbf{x}) = \int_\Omega G_\Delta(\mathbf{x},\mathbf{y})\phi(\mathbf{y})d\mathbf{y} \tag{4}$$

denotes spatial filtering of $\phi(\mathbf{x})$, $(\mathbf{x} \in \Omega)$ with nominal filter width Δ and tilde denotes Favre-filtered quantities; i.e. $\tilde{\phi} = \overline{\rho\phi}/\overline{\rho}$. As mentioned above, the shape of filter kernel $G_\Delta(\mathbf{x},\mathbf{y})$ is unknown for general unstructured grid. Nevertheless, we assume that the filtering is the mapping from the fully resolved solution to continuous representation of discrete solution with filter size $\Delta(\mathbf{x})$. $\tau_{ij} = \overline{\rho}(\widetilde{u_i u_j} - \widetilde{u}_i\widetilde{u}_j)$ and $q_k = \overline{\rho}\left(\widetilde{u_i T} - \widetilde{u}_i\overline{T}\right)$ are SGS stress and heat flux.

Equations (1) are discretized using collocated, or cell-centered finite volume method. The schematics for collocated FVM are shown in Fig. 1. Integrating over control volume CV and applying the Gauss theorem, Eq. (1) takes the form

$$\begin{aligned}
\frac{\partial \overline{\rho}_{\mathrm{cv}}}{\partial t} &= -\frac{1}{V_{\mathrm{cv}}}\sum_{\text{faces}}\overline{\rho}_f v_N A_f, \\
\frac{\partial\left(\overline{\rho}\widetilde{u}_i\right)_{\mathrm{cv}}}{\partial t} &= -\frac{1}{V_{\mathrm{cv}}}\sum_{\text{faces}}\left[\left(\overline{\rho}\widetilde{u}_i\right)_f v_N + \overline{p}_f n_i - \widetilde{\sigma_{ik}}_{,f} n_k + \tau_{ik,f} n_k\right] A_f, \\
\frac{\partial\left(\overline{E}_T\right)_{\mathrm{cv}}}{\partial t} &= -\frac{1}{V_{\mathrm{cv}}}\sum_{\text{faces}}\left[\left(\overline{E}_T + \overline{p}\right)_f v_N - \widetilde{\sigma_{ik}}_{,f}\tilde{u}_{i,f} n_k - \overline{Q}_{k,f} n_k + q_{k,f} n_k\right] A_f,
\end{aligned} \tag{5}$$

where V_{cv} is the volume of CV, A_f is the area of the face, n_i is the outward normal vector at surface, v_N is the face-normal velocity, and $\mathbf{q}_{\mathrm{cv}} = \left(\int_{\mathrm{cv}}\mathbf{q}dV\right)/V_{\mathrm{cv}}$ is the volume average within the cell, where $\mathbf{q} = \left(\overline{\rho}, \overline{\rho}\widetilde{u}_i, \overline{E}_T\right)$ is the conservative variable. Here, the subscript f denotes the interpolation at each face of CV. Discretization

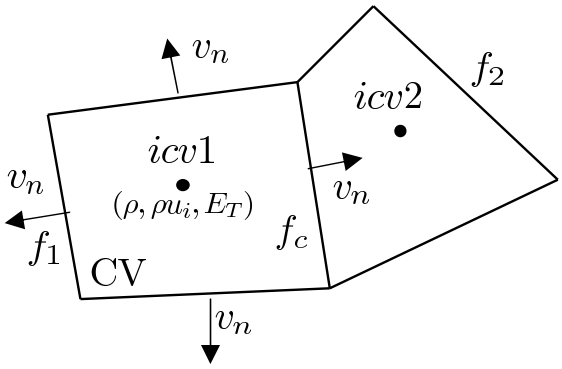

Figure 1. Schematic of the collocated scheme and parallel faces.

of the governing equation involves reconstruction of face values from cell center values. The emphasis of this paper is on the spatial discretization; the discretized system (5) is therefore advanced in time using the explicit Adams-Bashforth scheme to yield

$$q_j^{n+1} = q_j^n + \frac{\Delta t}{2}\left(3\mathrm{rhs}_j(\mathbf{q}^n) - \mathrm{rhs}_j(\mathbf{q}^{n-1})\right), \tag{6}$$

where rhs_j denotes j th component of r.h.s. of Eq. (5), and superscript n denotes n th time step.

In the subsequent sections, the effects of flux reconstruction, shock-capturing scheme and SGS models on the solution of (5) are investigated through various benchmark problems. Table 1 summarizes computational parameters of those problems. More detailed parameters, if necessary, will be described where they first appear in the paper.

III. Flux reconstruction at cell face

III.A. Convective flux

The spatial accuracy of the scheme is entirely dependent upon the "flux reconstruction" at the cell face from center values. It is known[5] that an interpolation that shows quadratic conservation (for divergencefree velocity) is the simple symmetric average

$$\phi_{f_c} = \frac{\phi_{icv1} + \phi_{icv2}}{2} \tag{7}$$

Table 1. Computational parameters of problems considered

problem def.	grid type (size)[a]	domain	flow type (SGS)	shock[b]	Re, M_∞
scalar equation	TET (1800)	$4 \times 1 \times 1$	scalar eqn.	No	N/A
vortex convection	HEX (32^3)	$(2\pi)^3$	Euler eqn.	No	N/A
Taylor-Green	HEX (32^3)	$(2\pi)^3$	laminar	No	10, 0.1
shock-tube	TET (38834)	$10 \times 2 \times 2$	laminar	Yes	1000, 1.2
shock-vortex	HEX (101×101)	10×10	laminar	Yes	1000, 1.2
mixing layer	HEX (81×81)/ TRI	30×100	laminar	Yes	1000, 0.8
isotropic turb.	HEX (32^3)	$(2\pi)^3$	turbulent (No)	Yes/No	100[c], 0.1
CBC[11]	HEX (32^3)/TET	$(2\pi)^3$	turbulent (Yes)	No	71[c], 0.1

a: HEX = hexahedral grid, TET=tetrahededral grid, TRI=triangular grid
b: shock capturing scheme (characteristic based filter), *c*: Taylor scale based initial Reynolds number

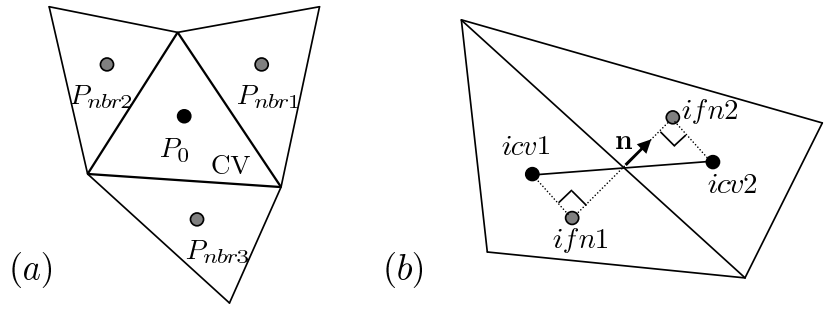

Figure 2. (a) Stencil for the computation of gradient and (b) schematic of computation of face normal gradient for viscous terms.

for any cell center variable ϕ, where f_c, $icv1$ and $icv2$ are illustrated in Fig. 1. In what follows, we will refer to Eq. (7) as the "symmetric average." In addition to (7), v_N should be given by means of projection to satisfy discrete continuity equation in order to guarantee the quadratic conservation in the inviscid, incompressible limit.[5] A compressible counterpart is recently proposed by Hou and Mahesh[4] based on the projection onto the energy equation. The Hou and Mahesh algorithm is fully implicit; however, since the focus of this paper is on spatial discretization, we consider the conventional interpolation-based method for $v_N = (\rho u_i)_f/\rho_f \cdot N_i$ and, thus, resulting scheme does not conserve the kinetic energy in the incompressible, inviscid limit.

In addition, this reconstruction is only first order accurate scheme for nonuniform grid. This may result in significant deterioration of the solution as will be shown later. An obvious choice for a better resolution is adding a gradient base term using Taylor series expansion at each cell to yield

$$\phi_{f_c} = \frac{\phi_{icv1} + \phi_{icv2}}{2} + \frac{1}{2}\left(\nabla\phi|_{icv1} \cdot \Delta\mathbf{x}^{icv1} + \nabla\phi|_{icv2} \cdot \Delta\mathbf{x}^{icv2}\right), \tag{8}$$

where $\Delta\mathbf{x}^{icv1} = \mathbf{x}_{f_c} - \mathbf{x}_{icv1}$, and $\nabla\phi|_{icv1}$denotes the gradient defined at $icv1$. We consider the following two approaches to obtain the gradient.

III.A.1. Least-square method (LSQ)

The first approach is called the 'least square method' (LSQ) since we develop $\nabla\phi|_{\rm cv}$ that can be used for the approximation of values at any adjacent points by

$$\phi(\mathbf{x}) \approx \phi(\mathbf{x}_0) + \nabla\phi|_{\rm cv} \cdot (\mathbf{x} - \mathbf{x}_0), \tag{9}$$

where $\mathbf{x}_0$ denotes coordinates of CV cell center, P_0 in Fig. 2, and $\mathbf{x}$ is any point that belongs to neighbor cells (see Fig. 2). Let $\nabla\phi|_{\rm cv} = (\mathcal{A}, \mathcal{B}, C)$, then the best choice of $\nabla\phi|_{\rm cv}$ is the one that minimizes the functional

$$F(\mathcal{A}, \mathcal{B}, C) = \sum_{\rm nbr} \left[\phi_{\rm nbr} - \phi(\mathbf{x}_0) - (\mathcal{A}, \mathcal{B}, C) \cdot (\mathbf{x}_{\rm nbr} - \mathbf{x}_0)\right]^2 w_{\rm nbr}, \tag{10}$$

where $\phi_{\rm nbr}$ and $\mathbf{x}_{\rm nbr}$ denote the values and locations of neighbor cells shown in Fig. 2. Here $w_{\rm nbr}$ is the weighting function, which is set to be 1 for simplicity and preserving symmetry of scheme. From the condition $\partial F/\partial\mathcal{A} = \partial F/\partial\mathcal{B} = \partial F/\partial\mathcal{C} = 0$, $\nabla\phi|_{\rm cv}$ is given by the solution of the system

$$\begin{bmatrix} \sum_{\rm nbr}\Delta x^2 & \sum_{\rm nbr}\Delta x\Delta y & \sum_{\rm nbr}\Delta x\Delta z \\ \sum_{\rm nbr}\Delta x\Delta z & \sum_{\rm nbr}\Delta y^2 & \sum_{\rm nbr}\Delta y\Delta z \\ \sum_{\rm nbr}\Delta x\Delta z & \sum_{\rm nbr}\Delta y\Delta z & \sum_{\rm nbr}\Delta z^2 \end{bmatrix} \begin{pmatrix} \mathcal{A} \\ \mathcal{B} \\ \mathcal{C} \end{pmatrix} = \begin{pmatrix} \sum_{\rm nbr}\Delta\phi_{\rm nbr}\Delta x \\ \sum_{\rm nbr}\Delta\phi_{\rm nbr}\Delta y \\ \sum_{\rm nbr}\Delta\phi_{\rm nbr}\Delta z \end{pmatrix}, \tag{11}$$

where $\Delta x = x_{\rm nbr} - x_0$, $\Delta\phi_{\rm nbr} = \phi_{\rm nbr} - \phi_0$ and other terms are defined similarly.

For a uniform one-dimensional grid with spacing Δx, LSQ reduces to a second order interpolation formula given by

$$\phi_{i+\frac{1}{2}} = \frac{1}{8}\left(-\phi_{i+2} + 5\phi_{i+1} + 5\phi_i - \phi_{i-1}\right), \tag{12}$$

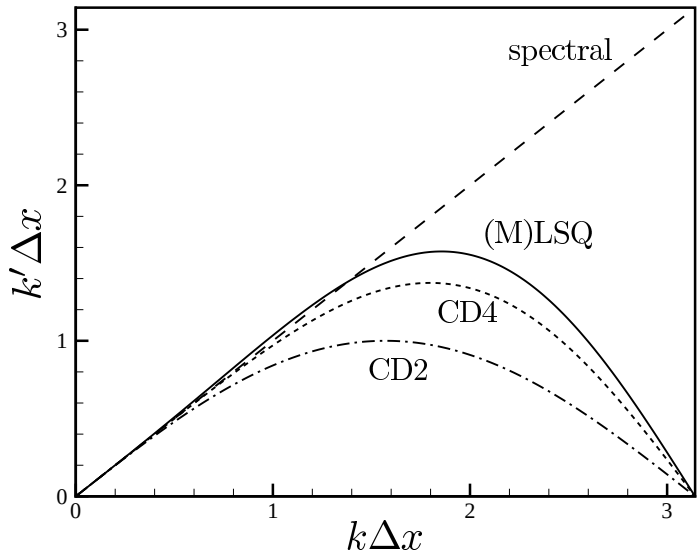

Figure 3. Modified wavenumbers for first derivative. Here, CD2 and CD4 denote second and fourth order central differences.

where $\phi_{i+1/2}$ is the value at cell face and ϕ_i, ϕ_{i+1}, ... are cell center values. The corresponding finite-difference is

$$\frac{\delta\phi}{\delta x} = \frac{-\phi_{i+2} + 6\phi_{i+1} - 6\phi_{i-1} + \phi_{i-2}}{8\Delta x}. \tag{13}$$

The scheme is formally second-order accurate. The modified wavenumber characteristics of this scheme is shown in Fig. 3, which clearly shows that resolution capability at high wavenumber is better than 4th order central difference scheme.

The LSQ scheme is first evaluated on the inviscid, vortex convection equation defined on a periodic box of $[0, 2\pi]^3$ domain. The initial condition is given as

$$\begin{aligned} u &= 1 - \frac{C(y-y_c)}{R^2}\exp(-r^2/2), \\ v &= \frac{C(x-x_c)}{R^2}\exp(-r^2/2), \\ p &= p_\infty - \frac{\rho C^2}{2R^2}\exp(-r^2), \end{aligned} \tag{14}$$

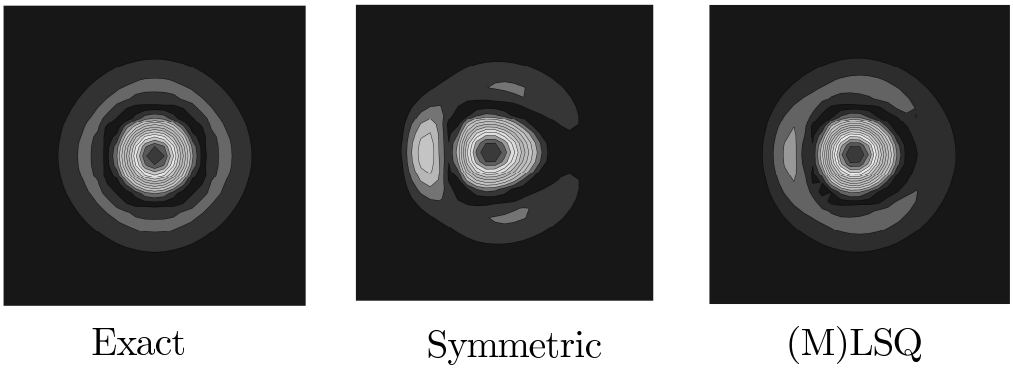

Figure 4. Vorticity contours at $t = 2\pi$ for inviscid vortex convection problem.

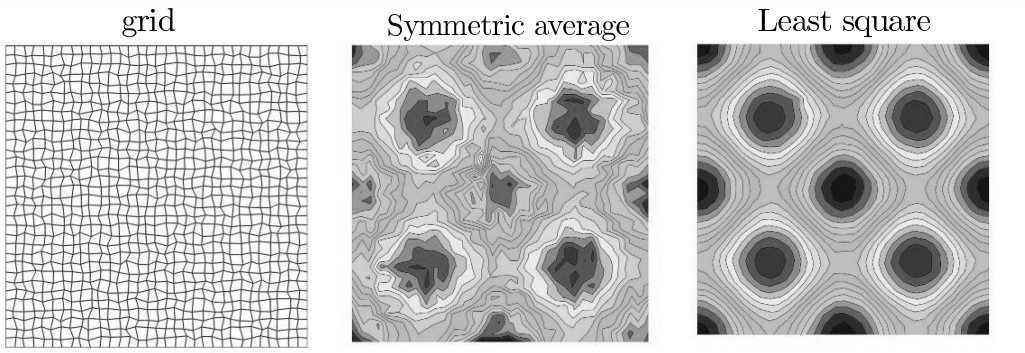

Figure 5. Grid and pressure contours at $t = 1.0$ from the Taylor-Green problem at $Re = 10$ and $M_\infty = 0.1$ with a perturbed haxahedral grid. Symbol, analytic solution; dashed, symmetric average; solid, least-square reconstruction.

where $r^2 = ((x - x_c)^2 + (y - y_c)^2)/R^2$. Here, $R = 1$, $C = 0.02$, $x_c = y_c = \pi$. Fig. 4 shows the vorticity contours at $t = 2\pi$ from exact solution, symmetric average and LSQ. As shown in Fig. 4, the large lagging phase due to the dispersion error is reduced by LSQ. Next, the Taylor-Green problem at $Re = 10$,$M_\infty = 0.1$ at a perturbed hexahedral grid (Fig. 5) is considered. See, e.g., Hou and Mahesh[4] for the initial condition and exact solution. Fig. 5 shows the decay of kinetic energy and pressure contour at $t = 2.0$. As shown, LSQ gives much more accurate prediction of pressure than the symmetric average. Next, highly under-resolved decaying isotropic turbulence is considered. The computation is performed at 32^3 resolution with initial micro-scale Reynolds number $Re_\lambda = u_{rms}\lambda/\nu = 100$, and the initial spectrum obeys

$$E(k) = 16\sqrt{\frac{2}{\pi}}\frac{u_0^2}{k_0}\left(\frac{k}{k_0}\right)^4 \exp\left(-2k^2/k_0^2\right), \tag{15}$$

where $k_0 = 5$ and $u_0 = 1$. Fig. 6 shows the decay of kinetic energy and the energy spectra at $t/t_e = 4$, where $t_e = \lambda/u_{rms}$ is the eddy turn-over time. As the reference solution, results from the dealiased pseudo-spectral method using the code described in Park and Mahesh[12] is also shown. Note that energy decay and spectra from LSQ are closer to those from the spectral method.

However, a serious instability of LSQ-reconstruction was observed on tetrahedral grids. Surprisingly, this instability is observed even for a linear problem where most schemes are Cauchy stable. As an example, the results from the scalar convection equation $\partial\phi/\partial t + \partial(U_j\phi)/\partial x_j = 0$ on a tetrahedral grid are shown in Fig. 7. Initial and boundary condition at the inlet ($x = -2$) are given by $\phi(x, 0) = 0.5$ and $\phi(-2, t) = 1$, respectively. As shown from Fig. 7(a), the solution diverges abruptly after $t > 0.4$.

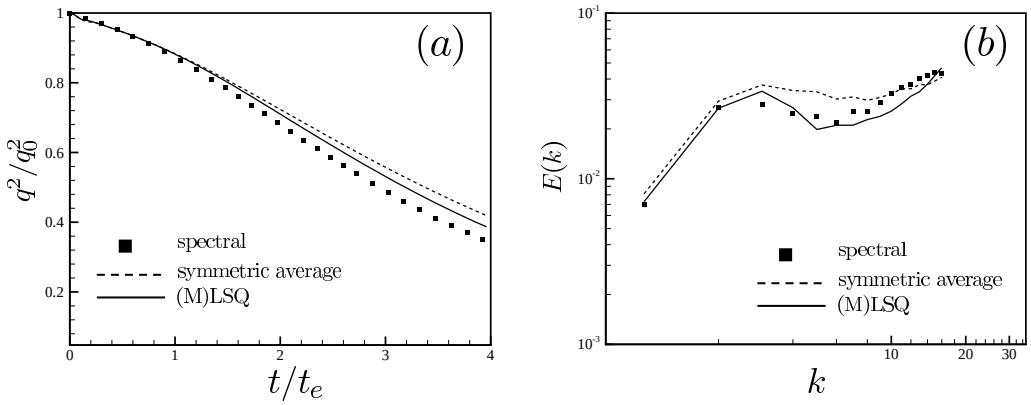

Figure 6. Effect of flux reconstruction scheme on the decaying isotropic turbulence at $Re_\lambda = 100$ on a hexahedral grid at 32^3 resolution.

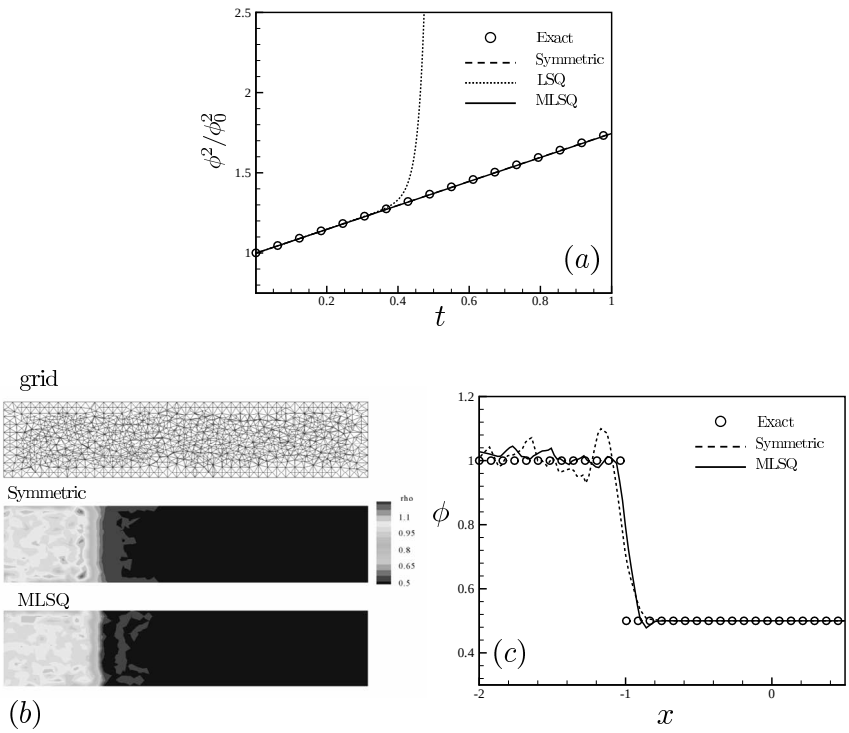

Figure 7. Stability and accuracy of high-resolution reconstruction: results from a scalar convection equation $\partial\phi/\partial t + \partial(U_j\phi)/\partial x_j$ with a tetrahedral grid. Shown are (a) time evolution of total ϕ^2, (b) grid and instantaneous contours of ϕ at $t = 1.0$, and (c) ϕ along $y = 0$ (center) at $t = 1.0$.

III.A.2. Modified least-square method (MLSQ)

An alternative way of defining the gradient is provided by the gradient theorem

$$\nabla\phi|_{\rm cv} = \frac{1}{V_{\rm cv}} \sum_{\rm faces} \phi^\star_{f_c} n_i A_f. \tag{16}$$

The main problem is Eq. (16) again requires the face value $\phi^\star_{f_c}$ which we are trying to estimate through Eq. (8). The superscript $\star$ is to discriminate this face value from ϕ_{f_c} in Eq. (8). This recursive relationship between gradients and face values is terminated simply by approximating $\phi^\star_{f_c} = 0.5(\phi_{icv1} + \phi_{icv2})$. The computed gradient from (16) is then inserted to (8) to obtain ϕ_{f_c}. It is easy to show that this method is identical to LSQ for uniform hexahedral grid, and thus has the same modified wavenumber characteristics as shown in Fig. 3. Even though this method does not use the idea of least-square error minimization, we will refer to it as the modified least-square (MLSQ) reconstruction for some reasons other than notational convenience that 1) it is considered as the alternative of LSQ, and 2) it stems from the same idea of Eq. (8), and 3) it reduces to LSQ for uniform grid.

The scalar convection equation mentioned above is again solved with MLSQ to get stable and more accurate result that that from the symmetric average as shown in Fig. 7. Note that results on vortex convection (Fig. 4) and decaying isotropic turbulence from LSQ are also those from MLSQ. Thus, it appears that MLSQ overcomes the instability problem of LSQ while keeping comparable accuracy. In what follows, all results that will be shown adopts MLSQ unless otherwise specified.

III.B. Viscous flux

In order to compute viscous flux vectors at cell face,

$$\widetilde{\sigma_{ij}}_{,f} = \left(\frac{\mu}{Re}\right)_f \left(\left.\frac{\partial \widetilde{u_i}}{\partial x_j}\right|_f + \left.\frac{\partial \widetilde{u_j}}{\partial x_i}\right|_f - \frac{2}{3} \left.\frac{\partial \widetilde{u_k}}{\partial x_k}\right|_f \delta_{ij} \right), \tag{17}$$

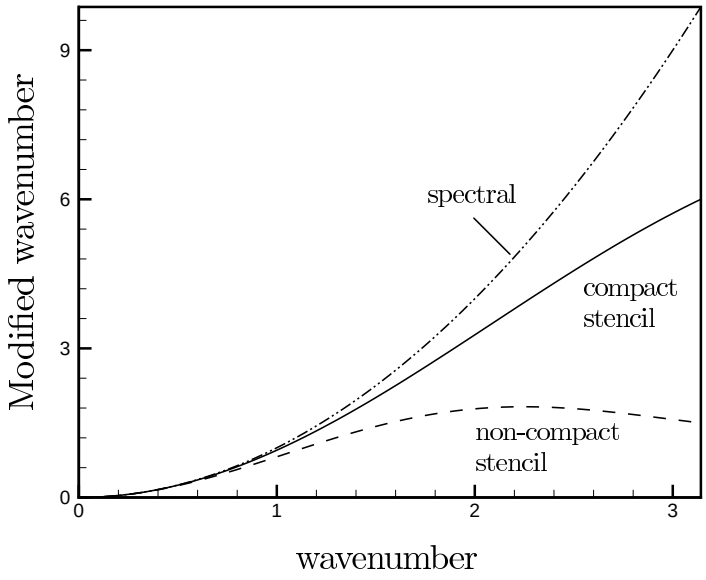

Figure 8. Three-dimensional modified wavenumbers for second derivative

all nine components of velocity deformation tensor $D_{ij} = \frac{\partial \widetilde{u_i}}{\partial x_j}$ should be defined at each cell face. This increases the computational overhead significantly. A simple remedy is to compute D_{ij} at cell centers and interpolate it at cell face by either symmetric average or (M)LSQ reconstruction. However, this approach is equivalent to get second derivative by double applications of first derivative, which results in non-compact stencil formulation. It is well known[12] that such method has much worse modified wavenumber characteristics than compact stencil methods, as illustrated in Fig. 8. In Fig. 8, three-dimensional modified wavenumbers[12] are shown for second order accurate, second derivatives realized by the double application of first derivative (non-compact) and compact approach, respectively.

In this paper, we make the trade-off by splitting $\widetilde{\sigma_{ij}} = \widetilde{\sigma}^1_{ij} + \widetilde{\sigma}^2_{ij}$ into two parts, where $\widetilde{\sigma}^1_{ij} = \frac{\mu}{Re}\frac{\partial \widetilde{u_i}}{\partial x_j}$ and $\widetilde{\sigma}^2_{ij} = \frac{\mu}{Re}\left(\frac{\partial \widetilde{u}_j}{\partial x_i} - \frac{2}{3}\frac{\partial \widetilde{u}_k}{\partial x_k}\delta_{ij}\right)$. $\widetilde{\sigma}^2_{ij}$ can be interpreted as the compressible part, since it vanishes in the incompressible limit. Then, r.h.s. of Eq. (5) that contains incompressible part, $\widetilde{\sigma}^1_{ij}$, is computed by

$$\frac{1}{V_{\rm cv}} \sum_{\rm faces} \left(\frac{\mu}{Re}\right)_f \left.\frac{\partial \widetilde{u_i}}{\partial x_j}\right|_f n_j A_f = \frac{1}{V_{\rm cv}} \sum_{\rm faces} \left(\frac{\mu}{Re}\right)_f \left.\frac{\partial \widetilde{u_i}}{\partial n}\right|_f A_f. \tag{18}$$

Here, the normal gradient at the face is computed by

$$\frac{\partial \phi}{\partial n} = \frac{\phi_{ifn2} - \phi_{ifn1}}{d_f}, \tag{19}$$

where $ifn1$ ($ifn2$) is the projection of $icv1$ ($icv2$) onto the extension of normal vector $\mathbf{n}$ as illustrated in Fig. 2, and d_f is the distance between $ifn1$ and $ifn2$. ϕ_{ifn1} is given by

$$\phi_{ifn1} = \phi_{icv1} + \nabla\phi|_{icv1} \cdot (\mathbf{x}_{ifn1} - \mathbf{x}_{icv1}), \tag{20}$$

where the least-square method, Eq. (11), is used to determine the gradient $\nabla\phi$ at $icv1$. Viscosity at the cell face is given by Eq. (8) and LSQ reconstruction. Thus, the incompressible part corresponds to compact-stencil method. Whereas, $\widetilde{\sigma}^2_{ij,f}$ is constructed by the interpolation of $\widetilde{\sigma}^2_{ij}\big|_{icv1}$ and $\widetilde{\sigma}^2_{ij}\big|_{icv2}$ using Eq. (8). Here again, the least-square method is used for all spatial derivatives at cell centers. Note that the least-square method does not raise any numerical instability for viscous flux vectors. Thus, the compressible part corresponds to non-compact scheme.

By using the proposed hybrid method, the computation of velocity deformation tensor at cell faces is avoided so that significant reduction of computational overhead is achieved. In terms of accuracy, the hybrid

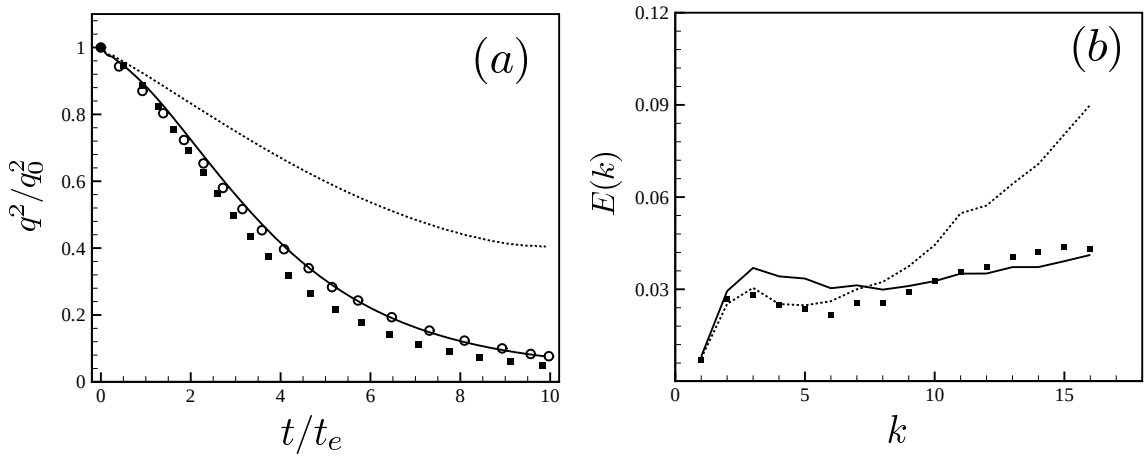

Figure 9. Effect of viscous term discretization on (a) kinetic energy decay and (b) energy spectra at $t/t_e = 4.0$ for a decaying isotropic turbulence at initial $Re_\lambda = 100$. Solid, compact viscous term; doted, non-compact viscous term; closed square, dealiased spectral; open circle, Hou and Mahesh.[4]

scheme is justified by the fact that viscous flux is dominated by incompressible part even with non-negligible compressibility. Since $\widetilde{\sigma}_{ij}^2$ is directly involved with the divergence, the compressible part becomes significant only in the vicinity of the shock, where most numerical dissipation is provided by shock-capturing scheme that will be described in the next section. Fig. 9 compares the kinetic energy decay and energy spectra from compact, and non-compact viscous flux discretization for the decaying isotropic turbulence at $Re_\lambda = 100$ described earlier. Here, the compact scheme denotes proposed hybrid scheme and non-compact scheme is achieved by the interpolation of both σ_{ij}^1 and σ_{ij}^2 from cell center values. For convective flux, symmetric average is adopted for the comparison with the existing result[4] on the structured grid. As shown, the agreement with result from structured grid is good for the case of compact method. On the other hand, results from non-compact method shows significantly slow decay of kinetic energy due to large pile-up of energy at high wavenumber region as expected from bad modified wavenumber characteristics in Fig. 8.

IV. Shock-capturing scheme

As mentioned in Sec. I, shock-capturing for non-dissipative schemes can be performed either by adding filter, or hybridization with upwind scheme. In the present study, we consider the filtering technique since the filter can be independently implemented with base scheme by predictor-corrector-like scheme described as follows. Once a physical time step Δt is advanced to get the solution $\hat{\mathbf{q}}^{n+1}$ from $\mathbf{q}^n$, the final solution $\mathbf{q}^{n+1}$ at $t + \Delta t$ is determined from a corrector-like scheme:[7]

$$\mathbf{q}_{\rm cv}^{n+1} = \hat{\mathbf{q}}_{\rm cv}^{n+1} - \frac{\Delta t}{V_{\rm cv}} \sum_{\rm faces} \left(\mathbf{F}_f^* \cdot \mathbf{n}_f \right) A_f, \tag{21}$$

where $\mathbf{F}_f^*$ is the filter numerical flux. Using this strategy, shock-capturing is easily isolated from the base scheme so that refinement of base scheme and shock capturing can be pursued independently. In this paper, the characteristic-based filter proposed for structured grids by Yee *et al.*[7] is generalized to unstructured grid. The main difficulty lies in the dependence on adjacent grid indices in the grid direction, and is realized on the unstructured grid by introducing two parallel faces f_1 and f_2 as represented in Fig. 1. Note that f_1 (f_2) is defined as the most parallel face to f_c among all the faces f that surrounds $icv1$ ($icv2$) except for f_c itself ($\equiv \{f\}_{icv1(icv2)}$). Practically, $f_1 \in \{f\}_{icv1}$ and $f_2 \in \{f\}_{icv2}$ are planes such that

$$\varphi(f,\, f_c) = 1 - \left| \mathbf{n}_{f_c} \cdot \mathbf{n}_f \right|. \tag{22}$$

has the minimum possible value.

Details of the implementation are as follows. The filter numerical flux has the form

$$\mathbf{F}^*_{f_c} = \frac{1}{2}\mathbf{R}_{f_c}\mathbf{\Phi}^*_{f_c}, \tag{23}$$

where $\mathbf{R}$ is the right Eigenvector of (convective flux vector) $= \left[\overline{\rho}_f v_N,\ (\overline{\rho}\tilde{u}_i)_f\, v_N + \overline{p}_f n_i,\ \left(\overline{E}_T + \overline{p}\right)_f v_N\right]^T$ $(i = 1,2,3)$ from Eq. (5). See, e.g., Rohde[13] for the complete expression. The face value $\mathbf{R}_{f_c} = \mathbf{R}(\mathbf{q}_{icv1}, \mathbf{q}_{icv2})$ is constructed using Roe's average:

$$\begin{aligned}
\mathbf{u}_{f_c,\mathrm{Roe}} &= \frac{\sqrt{\rho_{icv1}}\mathbf{u}_{icv1} + \sqrt{\rho_{icv2}}\mathbf{u}_{icv2}}{\sqrt{\rho_{icv1}} + \sqrt{\rho_{icv2}}}, \\
H_{f_c,\mathrm{Roe}} &= \frac{\sqrt{\rho_{icv1}}H_{icv1} + \sqrt{\rho_{icv2}}H_{icv2}}{\sqrt{\rho_{icv1}} + \sqrt{\rho_{icv2}}}, \\
c^2_{f_c,\mathrm{Roe}} &= (\gamma-1)\left[H_{\mathrm{roe}} - \frac{1}{2}\left(u^2_{f_c,\mathrm{Roe}} + v^2_{f_c,\mathrm{Roe}} + w^2_{f_c,\mathrm{Roe}}\right)\right],
\end{aligned} \tag{24}$$

where $H = (E_t + p)/\rho$ is the enthalpy and c is the speed of sound. On the other hand, the expression for the ℓ-th component of $\mathbf{\Phi}^*$, $\phi^{*\ell}$ is given by

$$\phi^{*\ell}_{f_c} = \kappa\theta^\ell_{f_c}\phi^\ell_{f_c}, \tag{25}$$

where κ is the adjustable parameter and θ_{f_c} is the switch function given by

$$\begin{aligned}
\theta_{f_c} &= \sqrt{0.5\left(\hat{\theta}^2_{icv1} + \hat{\theta}^2_{icv2}\right)}, \\
\hat{\theta}_{icv1} &= \left|\frac{|\alpha_{f_c}| - |\alpha_{f_1}|}{|\alpha_{f_c}| + |\alpha_{f_1}|}\right|^p, \\
\hat{\theta}_{icv2} &= \left|\frac{|\alpha_{f_2}| - |\alpha_{f_c}|}{|\alpha_{f_2}| + |\alpha_{f_c}|}\right|^p.
\end{aligned} \tag{26}$$

Here, $\alpha_f = \mathbf{R}_f^{-1}\Delta\mathbf{q} = \mathbf{R}_f^{-1}(\mathbf{q}_{icv2} - \mathbf{q}_{icv1})$ is the difference of the characteristic variable across the face, and $p = 1$ is used. Note that the formulation θ_{f_c} in Eq. (26) is a code-friendly variation of the original formulation[7] $\theta_{f_c} = \max\left(\hat{\theta}_{icv1}, \hat{\theta}_{icv2}\right)$ for the case $icv1$ and $icv2$ belong different processors in MPI-based parallel algorithm, and is proven to make a negligible difference with the original formulation.

For ϕ^ℓ, we choose the Harten-Yee TVD form

$$\phi^\ell_{f_c} = \frac{1}{2}\Psi\left(a^\ell_{f_c}\right)\left(g^\ell_{icv1} + g^\ell_{icv2}\right) - \Psi\left(a^\ell_{f_c} + \gamma^\ell_{f_c}\right)\alpha^\ell_{f_c}, \tag{27}$$

$$\gamma^\ell_{f_c} = \frac{1}{2}\frac{\Psi\left(a^\ell_{f_c}\right)\left(g^\ell_{icv2} - g^\ell_{icv1}\right)\alpha^\ell_{f_c}}{\left(\alpha^\ell_{f_c}\right)^2 + \epsilon}, \tag{28}$$

where $\epsilon = 10^{-7}$ and $\Psi(z) = \sqrt{\delta + z^2}$ $(\delta = 1/16)$ is introduced for the entropy fixing. $a^\ell_{f_c}$ is the element of the eigenvalues. According to Yee *et al.*,[7] g^ℓ_{icv}'s are cell center values defined in terms of α^ℓ_f's. One possible expression in the structured mesh is

$$g^\ell_{i,j,k} = \mathrm{minmod}\left(\alpha^\ell_{i,j-1/2,k},\ \alpha^\ell_{i,j+1/2,k}\right) \tag{29}$$

along j-direction. See Yee *et al.*[7] for other types of limiters. Equivalent definition holds for i- and k-directions. Therefore, there are three distinct values of $g^\ell_{i,j,k}$ according to the orientation of the faces under consideration. This fact brings about a significant problem in unstructured grid where the concept of the Cartesian direction does not exist. The best way to overcome this problem is to define g's at cell faces to account for this directional dependence. Since what we actually need are the symmetric average and difference, or $\frac{1}{2}\left(g_{icv1} + g_{icv2}\right)$ and $\frac{1}{2}\left(g_{icv2} - g_{icv1}\right)$, it is natural to define these quantities at cell faces:

$$g^{+\ell}_{f_c} \equiv \frac{1}{2}\left\{\mathrm{minmod}\left(\alpha^\ell_{f_1}, \alpha^\ell_{f_c}\right) + \mathrm{minmod}\left(\alpha^\ell_{f_c}, \alpha^\ell_{f_2}\right)\right\}, \tag{30}$$

$$g^{-\ell}_{f_c} \equiv \frac{1}{2}\left\{\mathrm{minmod}\left(\alpha^\ell_{f_2}, \alpha^\ell_{f_c}\right) - \mathrm{minmod}\left(\alpha^\ell_{f_1}, \alpha^\ell_{f_c}\right)\right\}. \tag{31}$$

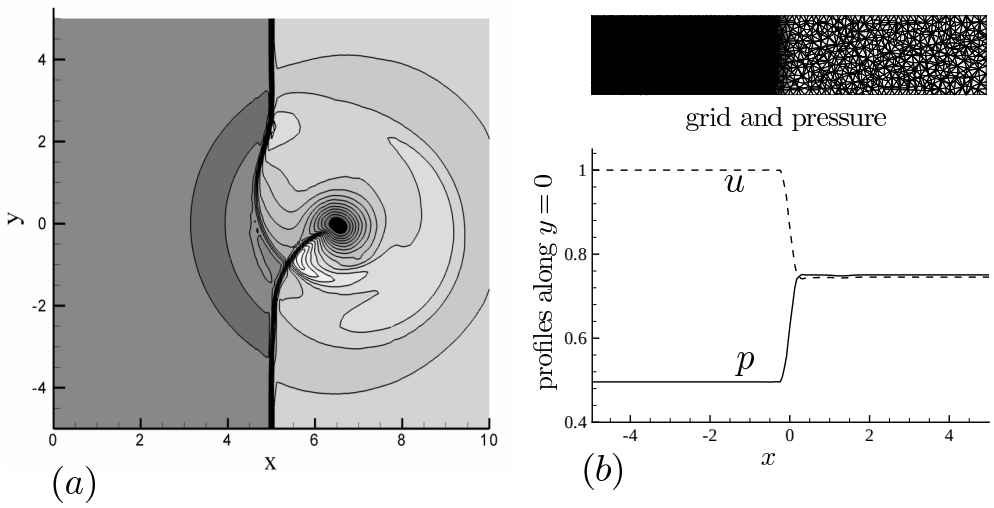

Figure 10. Performances of the characteristic-based filter. (a) pressure contours from a shock-vortex interaction at $t = 4.0$ with a uniform grid and (b) stationary shock tube problem with a tetrahedral grid.

Accordingly, $\phi^{\ell}_{f_c}$ and $\gamma^{\ell}_{f_c}$ are rewritten as follows:

$$\phi^{\ell}_{f_c} = \Psi\left(a^{\ell}_{f_c}\right) g^{+\ell}_{f_c} - \Psi\left(a^{\ell}_{f_c} + \gamma^{\ell}_{f_c}\right) \alpha^{\ell}_{f_c}, \tag{32}$$

$$\gamma^{\ell}_{f_c} = \frac{\Psi\left(a^{\ell}_{f_c}\right) g^{-\ell}_{f_c} \alpha^{\ell}_{f_c}}{\left(\alpha^{\ell}_{f_c}\right)^2 + \epsilon}, \tag{33}$$

The advantage of this three face-approach is that it does not use any interpolation between cell center and face values. Thus, this approach can guarantee the same result as what could be obtained from the original formulation, when the structured grid is used. The main concern about the parallel face approach lies in its feasibility on triangular and tetrahedral grids on which the appearance of 'not-so-parallel' parallel faces is unavoidable. Another concern is the problem of characteristic filtering itself that it depends on a tunable parameter κ. These are the main issues investigated by numerical tests.

Fig. 10 shows pressure contours from shock-vortex interaction and shock-tube problems. For both problems, $\kappa = 1.0$ is used. For shock-vortex interaction problem, a complete domain is shown in Fig. 10 which is discretized by a 101×101 uniform hexahedral grid. A vortex initially at $x = 3.0$ which is described by Eq. (14) with a stronger intensity ($C = 0.8$), interacts with a shock at $x = 5.0$ with $M = 1.2$. From Fig. 10, the basic performance of characteristic filter is excellent showing no oscillation near the shock and no smearing of vortex. The same conclusion is true for shock-tube problem for which a coarse tetrahedral grid is used as shown in Fig. 10. In spite of coarse resolution, the shock is captured within two grid points. Thus, it appears that parallel face approach is works well even for tetrahedral grids.

The next test case is a two-dimensional mixing layer at convective Mach number $M_c = 0.8$ and Reynolds number based on the vorticity thickness is 1000, which was intensively tested by Yee *et al.*[7] The main objective here is to investigate the performance of the shock capturing scheme on a triangular mesh shown in Fig. 11. For the purpose of comparison, computation is also performed on a 81×81 hexahedral grid which has a comparable resolution to the triangular grid. The base flow is $u = 0.5 \tanh(2y)$ and the initial perturbation is given by

$$v' = \sum_{k=1}^{2} a_k \cos\left(\frac{2\pi k x}{L_x} + \phi_k\right) \exp\left(-\frac{y^2}{b}\right), \tag{34}$$

where $a_1 = 0.05$, $a_2 = 0.01$, $\phi_1 = \phi_2 = -\pi/2$, $b = 10$ and $L_x = 30$. u' is determined from divergence-free condition. Temporal evolution of temperature contours are shown in Fig. 11 for both hexahedral and

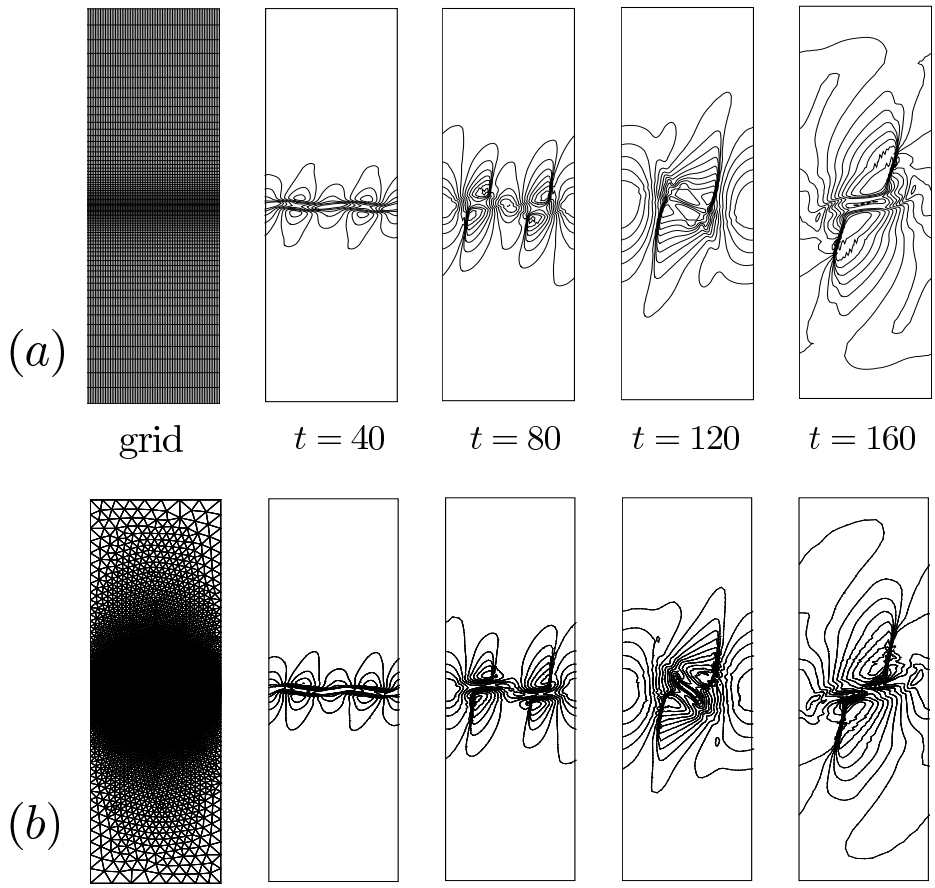

Figure 11. Temporal evolution of temperature contours for a time-developing mixing layer at $M_c = 0.8$ and $Re = 1000$ with (a) a hexahedral and (b) a triangular grid. Shown are 15 contours in the range of $0.8 \leq T/T_{ref} \leq 1.1$.

tetrahedral grids. Here, $\kappa = 0.3$ is applied for both cases. The formation of shocklets as well as the pairing and merging of vortex are well represented by both grids. Especially, good results from triangular grid again demonstrates the feasibility of the parallel face approach. Fig. 12 shows the effects of reconstruction accuracy, κ and the switch θ in Eq. (26). For this problem, it seems that the difference between symmetric average and MLSQ is small, because the flow is essentially laminar and well resolved except for the shock. Whereas, the increase of κ $(= 0.1)$ results in the smearing of the shock. Furthermore, both the vortex and and shock are smeared significantly when the Harten-Yee switch (Eq. (26)) is turned off by setting $\kappa\theta = 1$ as shown in Fig. 12 (d). Recall that without the Harten-Yee filter, or with $\phi^{*\ell}_{f_c} = \phi^{\ell}_{f_c}$, the characteristic based filter approaches a common TVD scheme. Therefore, Fig. 12 clearly shows the advantage of using the characteristic filter over TVD schemes.

However, when this filter is applied to an under-resolved turbulent problem, it is shown that the characteristic filter kills resolved-scale turbulence significantly even with small $\kappa = 0.1$ as shown in Fig. 13, where kinetic energy decay and energy spectra at $t/t_e = 4$ for the decaying isotropic turbulence at $Re_\lambda = 100$ are depicted. Thus, we consider the modification of the Harten-Yee filter with the idea of Ducros *et al.*[1] by multiplying the following sensor to θ_{f_c} in Eq. (26):

$$\theta^{\star}_{f_c} = \frac{1}{2}\left(\theta^{\star}_{icv1} + \theta^{\star}_{icv2}\right), \tag{35}$$

$$\theta^{\star}_{icv1} = \frac{(\nabla \cdot \mathbf{u})^2_{icv1}}{(\nabla \cdot \mathbf{u})^2_{icv1} + \Omega^2_{icv1} + \epsilon}, \tag{36}$$

where Ω is the vorticity magnitude and, here again, $\epsilon = 10^{-7}$ is a small positive value. $\theta^{\star}_{icv2}$ is defined

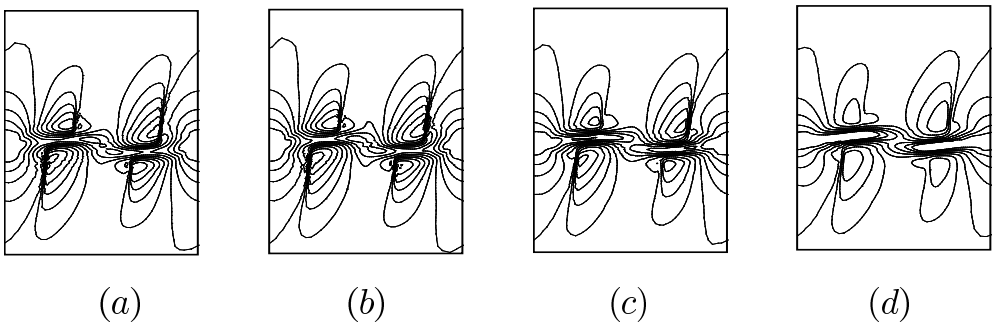

Figure 12. Temporal evolution of temperature contours for a time-developing mixing layer at $M_c = 0.8$ and $Re = 1000$ with a triangular grid: the effect of numerical parameters on the accuracy of the shock-capturing scheme. (a) MLSQ and $\kappa = 0.3$, (b) symmetric average and $\kappa = 0.3$, (c) MLSQ and $\kappa = 1.0$, (d) MLSQ and with no Harten-Yee switch.[7]

similarly to Eq. (36). As shown in Fig. 13, it is clear that proposed composite switch $\theta_{f_c} \cdot \theta^{\star}_{f_c}$ removes most of unnecessary dissipation even for considered under-resolved turbulence. Numerical tests (not shown here) indicates this switch preserves good shock-capturing capability of characteristic based filter. This behavior is readily imagined from the expected behavior of $\theta^{\star}_{f_x}$ which moves between 0 to 1: it approaches 1 only in the vicinity of shock and remains very small value close to 0 in other region.

V. Subgrid scale model

In this paper, we consider the compressible version of the dynamic Smagorinsky model[14] (DSM) and an one-equation model that uses SGS kinetic energy. In DSM, SGS stress and heat flux is modeled by

$$\tau_{ij} - \frac{\delta_{ij}}{3}\tau_{kk} = -2C_S(\mathbf{x},t)\overline{\rho}\Delta^2 \left|\tilde{S}\right| \widetilde{S^*_{ij}}, \tag{37}$$

$$\tau_{kk} = 2C_I(\mathbf{x},t)\overline{\rho}\Delta^2 \left|\tilde{S}\right|^2, \tag{38}$$

$$q_i = -\overline{\rho}\frac{C_S(\mathbf{x},t)\Delta^2 \left|\tilde{S}\right|}{Pr_T}\frac{\partial \overline{T}}{\partial x_i}, \tag{39}$$

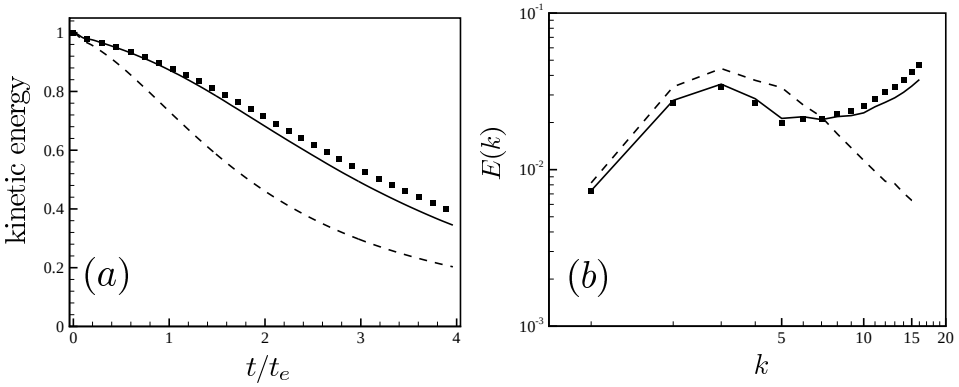

Figure 13. Effect of dissipation due to shock capturing scheme on (a) kinetic energy decay and (b) energy spectra at $t/t_e = 4.0$ for the isotropic turbulence with $Re_\lambda = 100$ and 32^3 hexahedral grid. Symbol, computation w/o shock capturing; dashed, Harten-Yee switch with $\kappa = 0.1$; solid, new composite switch with $\kappa = 0.1$.

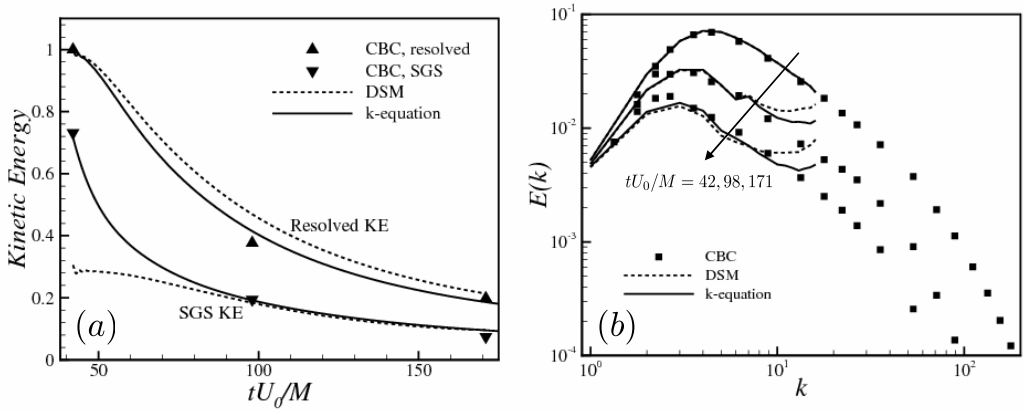

Figure 14. LES with DSM and one-equation model for the decaying isotropic turbulence[11] at 32^3 resolution. (a) Resolved and SGS kinetic energy; (b) energy spectra.

where $|S| = \sqrt{2S_{ij}S_{ij}}$ and $S^*_{ij} = S_{ij} - 1/3S_{kk}\delta_{ij}$. Model coefficients C_s, C_I and Pr_T are determined by the Germano identity. For example,

$$\begin{aligned} C_S\Delta^2 &= \frac{1}{2}\frac{\langle L^*_{ij}M^*_{ji}\rangle}{\langle M^*_{ij}M^*_{ji}\rangle}, \\ L_{ij} &= \left(\frac{\widehat{\overline{\rho u_i}\cdot\overline{\rho u_j}}}{\overline{\rho}}\right) - \frac{\widehat{\overline{\rho u_i}}\cdot\widehat{\overline{\rho u_j}}}{\widehat{\overline{\rho}}}, \\ M^*_{ij} &= \overline{\rho}\widehat{\left|\tilde{S}\right|\widetilde{S^*_{ij}}} - \widehat{\overline{\rho}}\left(\frac{\widehat{\Delta}}{\Delta}\right)^2\widehat{\left|\tilde{S}\right|}\widehat{\widetilde{S^*_{ij}}}, \end{aligned} \tag{40}$$

where, $\langle\cdot\rangle$ denotes spatial average over homogeneous direction(s) and caret denotes the test filtering. For unstructured gird, however, the detection of homogeneous direction is not straightforward. Thus, in the present study, this average is replaced by the filtering with a compact support, which is identical to the test filtering. Test filtering is defined by the linear interpolation from face values of a control volume, which is again the interpolation from two adjacent cell center values:

$$\widehat{\phi} = \frac{1}{N_{\text{face}}}\sum_{\text{no of face}}\phi_f = \frac{1}{2N_{\text{face}}}\sum_{\text{no of face}}(\phi_{icv1} + \phi_{icv2}), \tag{41}$$

where N_{face} is the number of faces for a given control volume. It is easy to show that (41) reduces to a discrete tophat filter for a structured hexahedral grid.

In addition to filtering and averaging, there some more fundamental issues in using DSM on unstructured grids. In incompressible flows, the subgrid kinetic energy is absorbed in the pressure. However, compressible flows require explicit modeling of the subgrid kinetic energy. As a result, we consider one-equation SGS model as an alternative to DSM that uses the transport equation of SGS kinetic energy $\overline{\rho}k = \frac{1}{2}(\widetilde{u_i u_i} - \tilde{u}_i\tilde{u}_i)$. The exact transport equation of SGS kinetic energy takes the form

$$\begin{aligned} \frac{\partial\overline{\rho}k}{\partial t} &= -\frac{\partial}{\partial x_j}(u_j\overline{\rho}k) + \frac{\partial}{\partial x_j}\left[\frac{1}{2}(\overline{\rho u_i u_i}\tilde{u}_j - \overline{\rho u_i u_i u_j}) + \frac{\mu}{3}\left(\overline{u_j\frac{\partial u_l}{\partial x_l}} - \tilde{u}_j\frac{\partial\tilde{u}_l}{\partial x_l}\right) + \overline{p}\tilde{u}_j - \overline{pu_j}\right] \\ &\quad + \frac{\partial}{\partial x_j}(\tilde{u}_i\tau_{ij}) - \tau_{ij}\tilde{S}_{ij} + \frac{\partial}{\partial x_j}\left(\mu\frac{\partial k}{\partial x_j}\right) - \mu\left(\overline{\frac{\partial u_i}{\partial x_j}\frac{\partial u_i}{\partial x_j}} - \frac{\partial\widetilde{u}_i}{\partial x_j}\frac{\partial\widetilde{u}_i}{\partial x_j}\right) \\ &\quad - \frac{\mu}{3}\left[\overline{\left(\frac{\partial u_l}{\partial x_l}\right)^2} - \left(\frac{\partial\tilde{u}_l}{\partial x_l}\right)^2\right] + \overline{p\frac{\partial u_l}{\partial x_l}} - \overline{p}\frac{\partial\tilde{u}_l}{\partial x_l}, \end{aligned} \tag{42}$$

where terms on the r.h.s. are convection, transport (triple correlation + dilatational diffusion + pressure diffusion), SGS diffusion, SGS dissipation, viscous diffusion, turbulent dissipation, dilatational dissipation,

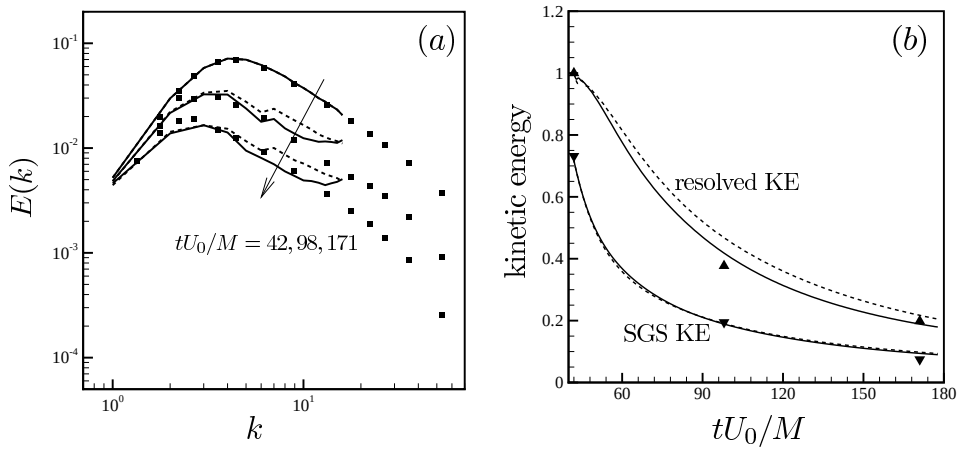

Figure 15. Effect of reconstruction scheme on (a) the energy spectra and (b) decay of resolved and SGS kinetic energy of the decaying isotropic turbulence on a 32^3 hexahedral grid. Symbols, Comte-Bellot & Corrsin;[11] dashed, symmetric average; solid, (M)LSQ. Here, k-equation model is considered.

and pressure-dilatation terms, respectively. Note that all dilatation-related terms are inherent in compressible flows. A general model for Eq. (42) can be written as

$$\frac{D\overline{\rho}k}{Dt} = \frac{\partial f_j}{\partial x_j} + \frac{\partial}{\partial x_j}\left(\tilde{u}_i\tau_{ij}\right) - \tau_{ij}\tilde{S}_{ij} + \frac{\partial}{\partial x_j}\left(\mu\frac{\partial k}{\partial x_j}\right) - \epsilon_s - \epsilon_c + \Pi, \tag{43}$$

where f_j, ϵ_s, ϵ_c, and Π denote models for transport, solenoidal dissipation, dilatational dissipation and pressure-dilatation, respectively. We consider the following models

$$f_j = C_f\overline{\rho}\Delta\sqrt{k}\frac{\partial k}{\partial x_j}, \tag{44}$$

$$\epsilon_s = C_{\epsilon s}\overline{\rho}k^{3/2}\Delta^{-1}, \tag{45}$$

$$\epsilon_c = C_{\epsilon c}M_t^2\overline{\rho}k^{3/2}\Delta^{-1} \tag{46}$$

$$\Pi = C_\Pi M_t^2\left(\frac{4}{3}\overline{\rho}k\frac{\partial\tilde{u}_l}{\partial x_l} + \tau_{ij}\tilde{S}_{ij}\right), \tag{47}$$

where $M_t = \sqrt{2k}/a$ is SGS turbulent Mach number, and C_f, $C_{\epsilon s}$, $C_{\epsilon c}$, and C_Π are closure coefficients. The above models mostly originate from RANS models for turbulence kinetic energy. Models for f_j and ϵ_s are similar to corresponding terms in incompressible model,[15] and models for dilatational dissipation ϵ_c and pressure-dilatation Π are from Sarkar *et al.*[16] and El Baz,[17] respectively. Therefore, Eqs. (43)-(47) can be also used as the one-equation model for RANS with a proper choice of closure coefficients.

In LES, unlike RANS, the model coefficients do not need to be specified a priori. Basically, we adopt the Germano identity to (44)-(47) to get those coefficients. Since all terms to be modeled take the form of $a = \overline{\alpha\beta} - \overline{\alpha}\,\overline{\beta}$, Germano identity $L = \widehat{\overline{\alpha}\,\overline{\beta}} - \widehat{\overline{\alpha}}\,\widehat{\overline{\beta}}$ always holds for a and its test-level representation $A = \widehat{\overline{\alpha\beta}} - \widehat{\overline{\alpha}}\,\widehat{\overline{\beta}}$. Since all models (44)-(47) take the form of $a^M = C\cdot m$, the coefficient C is determined by the minimization of the error

$$E = L - A^M - a^M = L - C(M - \widehat{m}) \tag{48}$$

in the least-square sense. By this procedure, for example, C_f is determined by

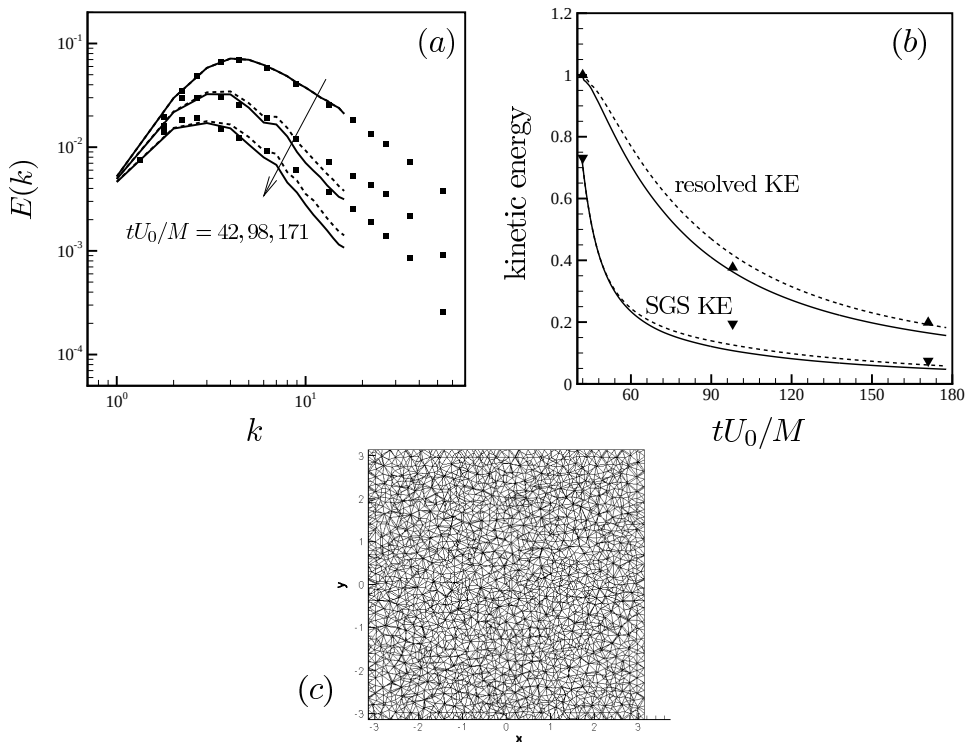

Figure 16. Effect of reconstruction scheme on (a) the energy spectr32^{3} hexaa and (b) decay of resolved and SGS kinetic energy of the decaying isotropic turbulence on a tetrahedral grid shown in (c). Symbols, Comte-Bellot & Corrsin;[11] dashed, symmetric average; solid, (M)LSQ. Here, k-equation model is considered.

$$
\begin{aligned}
C_f &= \frac{\left\langle (X_j - \hat{Y}_j) Z_j \right\rangle}{\left\langle (X_j - \hat{Y}_j)(X_j - \hat{Y}_j) \right\rangle}, \\
X_j &= \hat{\Delta}\hat{\overline{\rho}}\sqrt{K}\partial_j K, \;\; Y_j = \Delta\overline{\rho}\sqrt{k}\partial_j k, \\
Z_j &= \widehat{\tilde{u}_j(\overline{p} + \overline{\rho}k + \overline{\rho}\tilde{u}_i\tilde{u}_i/2)} - \tilde{u}_j(\overline{p} + \overline{\rho k + \overline{\rho}\tilde{u}_i\tilde{u}_i/2}),
\end{aligned}
\tag{49}
$$

where $K = \hat{k} + \frac{1}{2}\tilde{u}_i\tilde{u}_i$ is sub-test scale kinetic energy. $C_{\epsilon c}$ and C_Π are determined similarly. Although there is a similar dynamic procedure for $C_{\epsilon s}$, it is highly erroneous since the term in the Germano identity composed of resolved scale viscous dissipation is vanishingly small, as noted by Ghosal *et al.*[15] Instead, constant value $C_{\epsilon s} = 1.0$ is used in the present study.

Note that for a quasi-incompressible flow where SGS dilatational terms are negligible, Eqs. (43)-(47) reduces to

$$
\frac{D\overline{\rho}k}{Dt} = -\tau_{ij}\widetilde{S}_{ij} - C_\epsilon \overline{\rho} k^{3/2}\Delta^{-1} + \frac{\partial}{\partial x_j}\left(\tilde{u}_i\tau_{ij}\right) + \frac{\partial}{\partial x_j}\left(C_f\Delta\overline{\rho}\sqrt{k}\frac{\partial k}{\partial x_j}\right) + \frac{\partial}{\partial x_j}\left(\frac{\mu}{Re}\frac{\partial k}{\partial x_j}\right). \tag{50}
$$

This is the same as k-equation model due to Ghosal *et al.*[15] except that the third term on the RHS, SGS transport term, has been ignored in Ghosal *et al.*'s paper following the convention of RANS. However, recent *a priori* test[18] revealed that this term is as large as SGS dissipation and thus plays significant role in redistribution of SGS kinetic energy.

The modeled SGS stress now takes the form

$$
\tau_{ij} - \frac{2}{3}k\delta_{ij} = -2C\Delta\overline{\rho}\sqrt{k}\tilde{S}_{ij}. \tag{51}
$$

Here, C is again determined through the dynamic procedure mentioned above.

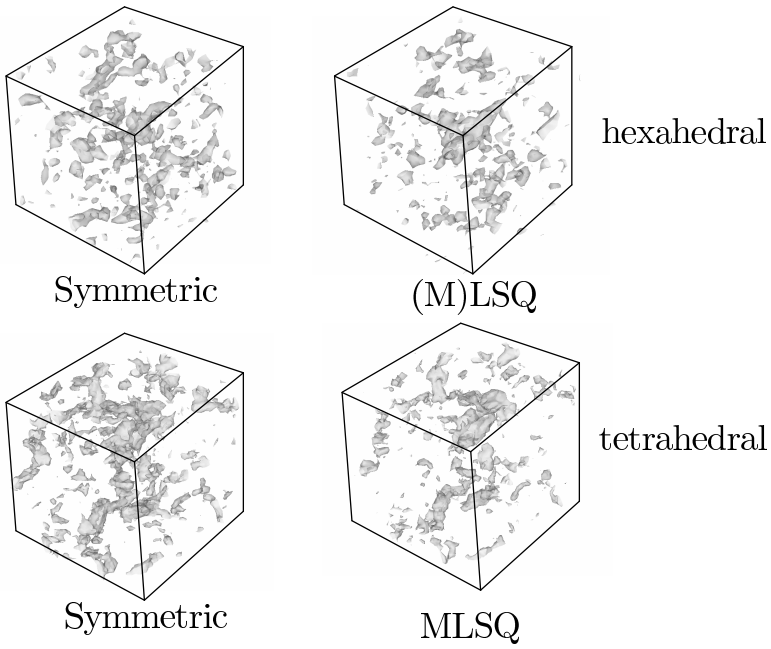

Figure 17. Iso-contours of $u^{'}/u_0^{'} = 0.5$ at $tU_0/M = 171$ from LES with hexahedral (upper) and tetrahedral (lower) grids using symmetric average (left) and (M)LSQ (right).

The performances of DSM and proposed dynamic k-equation model are tested on Comte-Bellot & Corrsin (CBC)[11] isotropic turbulence at 32^3resolution of uniform hexahedral grid (Fig. 14). For one-equation model, a uniform value is given as the initial SGS kinetic energy such that total value matches the experimental data. As shown in Fig. 14, the results from one-equation model is quite encouraging that both resolved and SGS kinetic energy as well as energy spectra are accurately predicted. Whereas, the Yoshizawa model[14] (38) shows large discrepancy in the initial stage and DSM shows lack of SGS dissipation possibly due to non-sharpness of shape of test filter in the wavespace that leads to smaller model coefficient than that from cutoff filter.[19]

Figs. 15 shows the effect reconstruction schemes on the energy spectra and time evolution of resolved and SGS kinetic energy. Here, k-equation model is considered. Spectra from symmetric average overpredicts energy at intermediate wavenumbers and thus overpredicts resolved kinetic energy. The shape of spectrum and overpredicton of resolved kinetic energy agrees very well with EDQNM prediction on second order schemes and spectral simulation with modified wavenumbers.[12] The same computation is performed on a tetrahedral grid at comparable resolution (see Fig. 16(c) for the grid), and results are shown in Fig. 16. The relationship between symmetric average and MLSQ is the same for tetrahedral grid, and MLSQ gives better prediction for resolved kinetic energy. It should be also mentioned that here we considered only quasi-incompressible isotropic turbulence so that we were unable to assess proposed models for dilatational dissipation (Eq. (46)) and pressure-dilatation (Eq. (47)) properly: they are smaller than other terms by orders of magnitude. The validation of those models and the effect of adding SGS transport term are subjects of future research.

VI. Conclusion

This paper deals with some important numerical and modeling issues that arise from using non-dissipative, cell-centered FVM for LES of compressible flows on unstructured grid, which are the accuracy and stability of flux interpolation scheme, shock capturing strategy and the implementation of SGS model. To enhance the accuracy of flux reconstruction, a new scheme with added first derivative term from each cell center is considered, whose accuracy is determined by that of gradient at cell center. First, the least-square based method is applied to get the gradient. This scheme enhances the accuracy of the scheme for hexahedral

grid, but a severe instability is observed for tetrahedral grid. Thus, modification to this scheme is proposed using the gradient theorem and the symmetric average. The proposed scheme is shown to be stable for all test problems considered, while preserving the accuracy of the least-square reconstruction. For viscous flux, an efficient method is proposed which guarantees compact stencil discretization in the incompressible limit. As a shock-capturing method, a characteristic based filter[7] is reformulated and implemented as a suitable form for the current cell centered FVM. Toward this end, two parallel faces are introduced at each face, and this approach is successful even for tetrahedral and triangular grids where parallel faces are less clear than hexahedral grid. However, characteristic based filter is shown to be overly dissipative for turbulence simulation, killing under-resolved turbulence fluctuations. As a remedy, another switch which detects the local divergence and vorticity[1] is multiplied to the characteristic filter. Finally, the filtering and averaging issues in implementing dynamic Smagorinsky model on unstructured grid is discussed. As an alternative, one-equation model using subgrid scale kinetic energy transport equation is proposed, and shown to achieve better results for a decaying isotropic turbulence than those from DSM.

Acknowledgments

This work was supported by the Department of Energy under the Stanford ASC alliance, and the Air Force Office of Scientific Research under grant FA9550-04-1-0341. Computer time was provided by the Minnesota Supercomputing Institute, the San Diego Supercomputer Center, and the National Center for Supercomputing Applications. We are thankful to Dr. Suman Muppidi for useful discussions.

References

[1]F. Ducros, V. Ferrand, F. Nicoud, C. Weber, D. Darracq, C. Gacherieu and T. Poinsot, 1999, Large-eddy simulation of the shock/turbulence interaction, *J. Comput. Phys.* **152**: 517.

[2]R. Mittal and P. Moin, 1997, Suitability of upwind-biased finite-difference schemes for large-eddy Simulation of Turbulent Flows, *AIAA J.* **35**: 1415.

[3]N. Park, J. Y. Yoo and H. Choi, 2004, Discretization errors in large eddy simulation: on the suitability of centered and upwind-biased compact difference schemes, *J. Comput. Phys.* **198**: 580.

[4]Y. Hou and K. Mahesh, 2005, A robust colocated implicit algorithm for direct numerical simulation od compressible turbulent flows, *J. Comput. Phys.* **205**: 205.

[5]K. Mahesh, G. Constantinescu and P. Poin, 2004, A numerical method for large-eddy simulation in complex geometries, *J. Comput. Phys.* **197**: 215.

[6]A. Jameson, W. Schmidt and E. Turkel, 1981, Numerical solution of the Euler equation by finite volume methods using Runge-Kutta time stepping scheme, *AIAA Paper* 81-1259.

[7]H. C. Yee, N. D. Sandham and M. J. Djomehri, 1999, Low-dissipative high-order shock-capturing methods using characteristic-based filters, *J. Comput. Phys.* **150**: 199.

[8]N. A. Adams, 1998, Direct numerical simulation of turbulent compression ramp flow, *Theoret. Comput. Fluid Dyn.* **12**: 109.

[9]K. Mahesh, S. K. Lele and P. Moin, 1997, The influence of entropy fluctuations on the interaction of turbulence with a shock wave, *J. Fluid Mech.* **334**: 353.

[10]M. Germano, U. Piomelli, P. Moin and W. Cabot, 1991, A dynamic subgrid-scale eddy viscosity model, *Phys. Fluids A* **3**: 1760.

[11]G. Comte-Bellot and S. Corrsin, 1971, Simple Eulerian time correlation of full- and narrow-band velocity signals in grid-generated, 'isotropic' turbulence, *J. Fluid Mech.* **48**: 273.

[12]N. Park and K. Mahesh, 2006, Analysis of numerical errors in large eddy simulation using statistical closure theory, *J. Comput. Phys.,* In press.

[13]A. Rohde, 2001, Eigenvalues and Eigenvectors of the Euler equations in general geometries, *AIAA paper* 2001-2609.

[14]P. Moin, K. Squires, W. Cabot and S. Lee, 1991, A dynamic subgrid-scale model for compressible turbulence and scalar transport, *Phys. Fluids* A**3**: 2746.

[15]S. Ghosal, T. S. Lund, P. Moin and K. Akselvoll, 1995, A dynamic localization model for large-eddy simulation of turbulent flows, *J. Fluid Mech.* **286**: 229.

[16]S. Sarkar, G. Erlebacher, M. Y. Hussaini, and H. O. Kreiss, 1991, The analysis and modelling of dilatational terms in compressible turbulence, *J. Fluid Mech.* **227**: 473.

[17]A. M. El Bbaz, 1992, Modelling compressibility effects on free turbulent shear flows, *5th Biennial Colloquium on Computational Fluid Dynamics*, University of Manchester Institute of Science and Technology, Manchester, England, U. K, 27-28. May 1992.

[18]C. B. da Silva and O. Metais, 2002, On the influence of coherent structures upon interscale interactions in turbulent plane jets, *J. Fluid Mech.* **473**: 103.

[19]E. T. Spyropoulos and G. A. Blaisdell, 1996, Evaluation of the dynamic model for simulation of compressible decaying isotropic turbulence, *AIAA J.* **34**: 990.